



Fe, Cu-decorated carbon material produced from ionic liquids as resourceful electrocatalyst for water splitting

Jelena Georgijević^a, Jadrinka Milikić^b, Yasemin Aykut^c, Nikola Zdolšek^a, Diogo M.F. Santos^d, Ayşe Bayrakçeken^c, Biljana Šljukić^{b,d,*}

^a Department of Physical Chemistry, "Vinča" Institute of Nuclear Sciences—National Institute of the Republic of Serbia, University of Belgrade, Mike Petrovića Alasa 12-14, 11351 Belgrade, Serbia

^b University of Belgrade, Faculty of Physical Chemistry, Studentski trg 12-16, 11158 Belgrade, Serbia

^c Department of Chemical Engineering, Atatürk University, Erzurum, Turkey

^d Center of Physics and Engineering of Advanced Materials, Laboratory for Physics of Materials and Emerging Technologies, Chemical Engineering Department, Instituto Superior Técnico, Universidade de Lisboa, 1049-001 Lisbon, Portugal

ARTICLE INFO

Keywords:

Oxygen evolution reaction
Hydrogen evolution reaction
Transition metal
Iron
Copper

ABSTRACT

The quest for highly efficient, stable, and economically viable bifunctional electrocatalysts is of paramount relevance for advancing in water splitting for the hydrogen energy sector, particularly in facilitating hydrogen (HER) and oxygen evolution evolution (OER) as cathodic and anodic reaction, respectively. In this study, two ionic liquids containing transition metal Fe or Cu, as well as a mixture of these ionic liquids, were used as precursors to synthesize Fe-, Cu-, and Fe,Cu-decorated carbon materials through simple, straightforward, and inexpensive carbonization processes. Comprehensive characterization via SEM-EDS, TEM, XRD, and XPS established the formation of Fe_3O_4 and Cu_2O species. These materials were systematically evaluated for OER and HER in alkaline electrolyte. Fe,Cu-decorated carbon electrocatalyst exhibited favorable performance for OER, including a low onset potential, and reaching 10 and 50 mA cm^{-2} at overpotential values of 325 mV and 364 mV, respectively. Notably, grafting both Fe and Cu in the material further augmented its electrocatalytic properties, underscoring the enhanced potential of transition metal-decorated carbon materials for OER applications.

1. Introduction

Society faces high demand for pure hydrogen (H_2) as high-energy density and green energy carrier [1]. The most popular application of H_2 is in fuel cells, as a pollution-free fuel. Still, H_2 also has widespread applications in different industries (e.g., oil refining, steel industry) and medicine [2]. Therefore, increasing the production of H_2 is an imperative where production must fulfill all green chemistry principles. Currently, H_2 is mainly produced under harsh conditions and energy-consuming methods, leading to environmental pollution. Water splitting driven by renewable energy would enable production of green H_2 [3–5]. Therefore, electrolytic splitting of water represents the most sustainable method for H_2 generation in the future [6]. During this process, two half-reactions occur at the electrolyzer's electrodes: hydrogen evolution reaction (HER) at the cathode and oxygen evolution reaction (OER) at the anode. Still, electrolytic water splitting does not have an

extensive industrial-scale application, mainly due to the issues associated with the energy efficiency of electrolyzers. High energy efficiency could be achieved by developing new electrocatalysts for two half-reactions [7]. Pt-based materials and Ru and Ir oxides are the state-of-the-art catalysts for evolution of hydrogen and oxygen, respectively [8]. However, due to their low abundance and consequent high prices, Pt, Ru, and Ir are not applicable at large scale. Besides introducing novel Pt-group metal-based electrocatalysts [9,10], notable progress in this field was made by introducing nonprecious electrocatalysts [11,12]. The most explored metals are transition metals Fe, Ni, Co, Cu, and Mn and their compounds [13], alloys [14,15], oxides [16], carbides [17], phosphides [18], borides [19], etc. Still, these electrocatalysts often showed lower electrocatalytic performance as well as poorer stability. These drawbacks were attributed to their surface electronic structure, morphological and textural properties, crystallinity and/or composition. Carbon materials are also finding potential applications as

* Corresponding author at: Center of Physics and Engineering of Advanced Materials, Laboratory for Physics of Materials and Emerging Technologies, Chemical Engineering Department, Instituto Superior Técnico, Universidade de Lisboa, 1049-001 Lisbon, Portugal.

E-mail address: biljana.paunkovic@tecnico.ulisboa.pt (B. Šljukić).

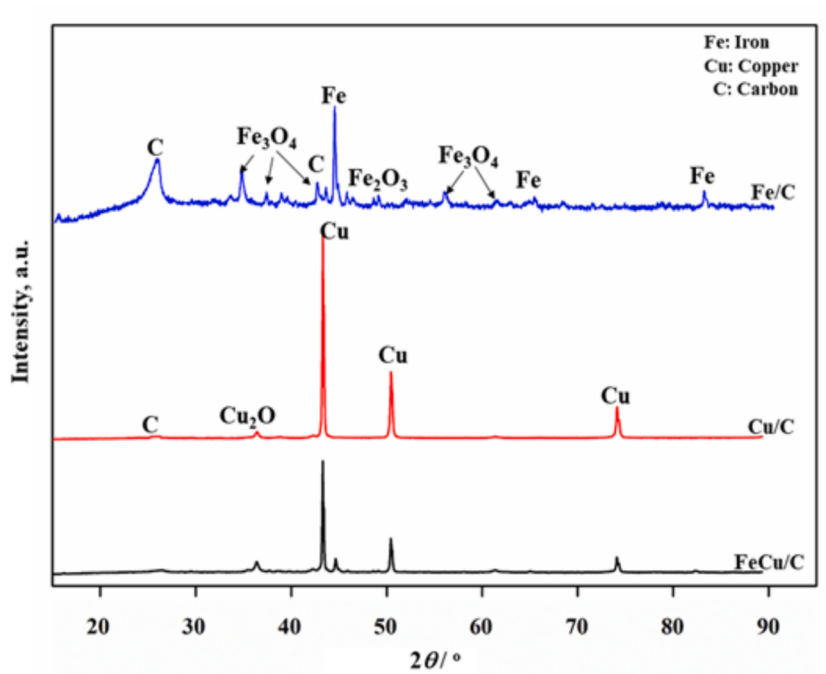


Fig. 1. XRD patterns of the Fe/C, Cu/C, and Fe,Cu/C catalysts.

electrocatalysts for HER and OER.

The rational design of electrocatalysts utilizing transition metals and carbon materials for efficient water splitting aims to achieve several objectives [13]: (i) enhancement of the active sites density by increasing the specific surface area to prevent metal nanoparticles aggregation; this further promotes efficient adsorption of water and H/OH species for rapid H₂/O₂ gas evolution, (ii) modification of the electronic structure by increasing the electrocatalyst's electronegativity; (iii) improvement of conductivity and facilitation of the electron/mass transfer ability through a close interface between transition metal and carbon support; this is achieved by adjusting the carbon support thickness and the metal constituent amount, which reduces diffusion distance for reactants and intermediates.

Thus, besides low cost and relative simplicity, a novel synthesis method for carbon materials could offer the possibility of preparing carbons with tuneable physicochemical properties. Preparing carbon materials with adequate electronic structure, morphology, and compositions could solve existing electrocatalysts' drawbacks. An easy, one-step method for preparing carbons is using ionic liquids (ILs), organic compounds rich in carbon atoms, as precursors [20–23]. Additionally, ILs are thermally stable compounds (decomposition usually starts > 400 °C) with negligible vapor pressure; this makes them perfect candidates for porous carbon precursors with a relatively high yield of material. Moreover, the remarkable diversity in the chemical compositions of ILs, along with the presence of various heteroatoms in their molecular structure, opens up the possibility of synthesizing carbon materials doped with a wide range of other atoms, including nitrogen (N), sulfur (S), and even metals [20–23]. Also, different chemical structures of ILs results in the formation of unique carbon morphologies. In summary, the diversity of chemical compositions and heteroatoms present in ILs not only enables the doping of carbon materials with a wide range of elements, but also different chemical structures lead to variations in carbon morphology. Such versatility in tailoring the properties of carbon materials through IL-based synthesis holds tremendous potential for driving innovation and breakthroughs in multiple fields, from energy storage and catalysis to electronics and beyond.

Herein, for the first time, two transition metal (Fe and Cu)-containing ionic liquids based on 1-butyl-3-methylimidazolium chloride were used

for the synthesis of Fe- and Cu-decorated carbon, as well as Fe,Cu-decorated carbon material. The three materials were investigated as bifunctional catalysts for electrolytic water splitting, *i.e.*, for HER and OER.

2. Experimental

2.1. Synthesis of ionic liquids and carbon materials

Two ionic liquids based on 1-butyl-3-methylimidazolium chloride ([Bmim]Cl, Sigma Aldrich), CuCl₂ (Zorka Šabac), and FeCl₂ (Centrohem) were used to prepare the carbon materials. The ILs were prepared without solvent, using an appropriate amount of [Bmim]Cl and metal chloride at 80 °C in argon atmosphere, according to the reactions described in Eqs. (1) and (2).



Immediately after mixing the reactants, viscous liquids were formed. Obtained ILs were dried under vacuum using a rotary evaporator.

Using these two ILs: ([Bmim]₂[CuCl₄] and [Bmim]₂[FeCl₄]) as precursors, three carbon materials were prepared: Cu-decorated carbon, Fe-decorated carbon, and Fe,Cu-decorated carbon. For the preparation of Fe,Cu-decorated carbon material, a mixture of [Bmim]₂[CuCl₄] and [Bmim]₂[FeCl₄] in weight ratio 1:1 was used as a carbon precursor. Carbonization was performed in a tube furnace (Protherm, Ergazi Mah, Ankara, Turkey) equipped with an alumina tube. Carbon precursors were carbonized at 800 °C, at a heating rate of 10 °C min⁻¹, and nitrogen flow rate of 2 mL min⁻¹. After reaching 800 °C, materials were kept at that temperature for 1 h and, subsequently, were left to cool down to room temperature under constant nitrogen flow. Experimental details of structural characterization and electrochemical studies are given in Supplementary information (SI).

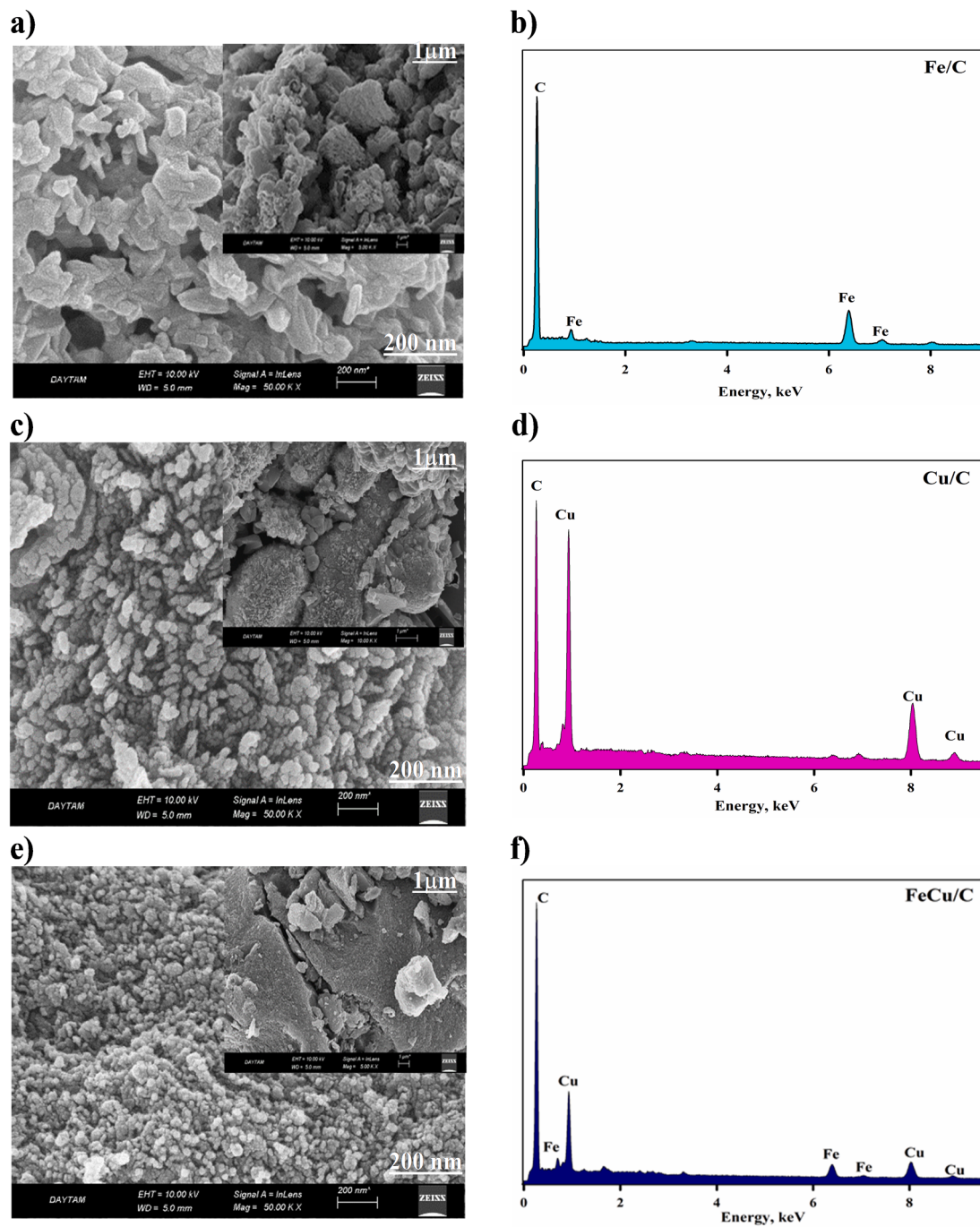


Fig. 2. SEM images and EDS analysis results of synthesized catalysts. (a,b) Fe/C, (c,d) Cu/C, and (e,f) Fe,Cu/C.

3. Results and discussion

3.1. Physicochemical characterization

The X-ray diffractograms of the synthesized catalysts are given in Fig. 1. The peak at a $2\theta < 30^\circ$ seen for all catalysts is attributed to the (002) plane of hexagonal graphite crystal structure of the carbon [24]. It could be seen that the peak intensity of the C (002) plane of Fe/C is higher than the other catalysts. In addition, the peak at 2θ of 42° , clearly visible in diffractogram of the Fe/C, corresponds to a reflection from C (100) plane of a hexagonal graphite crystal structure [25,26]. The diffractograms of Fe-based catalysts show peaks at 44.57, 65.37, and 81.7° corresponding to reflections from (110), (200), and (211), respectively, of body-centered cubic (bcc) structure of the Fe. Other peaks seen

in the Fe/C diffractogram are related to the presence of iron oxide structures. Namely, the diffraction peaks at 2θ of 35.45, 37.89, 43.09, 56.99, and 62.68° are attributed to (311), (222), (400), (511), and (440) planes, respectively, of Fe_3O_4 in the cubic phase. Moreover, the distinctive peaks at 40.88 and 49.51° of Fe/C are attributed to the (113) and (024) planes, respectively, compatible with Fe_2O_3 of rhombus-centered hexagonal structure [27–29]. Diffractogram of Cu/C displays peaks at 2θ of 43.28, 50.40, and 74.81° that correspond to the planes (111), (200), and (220), respectively, of the face-centered cubic (fcc) structure of Cu. Among these peaks, that at 2θ of 43.28° showed the strongest intensity. Moreover, the diffraction peak at 36.37° is attributed to the (111) plane of Cu_2O [30,31]. On the other hand, the peaks observed for Fe,Cu/C are compatible with those of Fe and Cu nanoparticles. No shift was observed in 2θ values of these metals suggesting

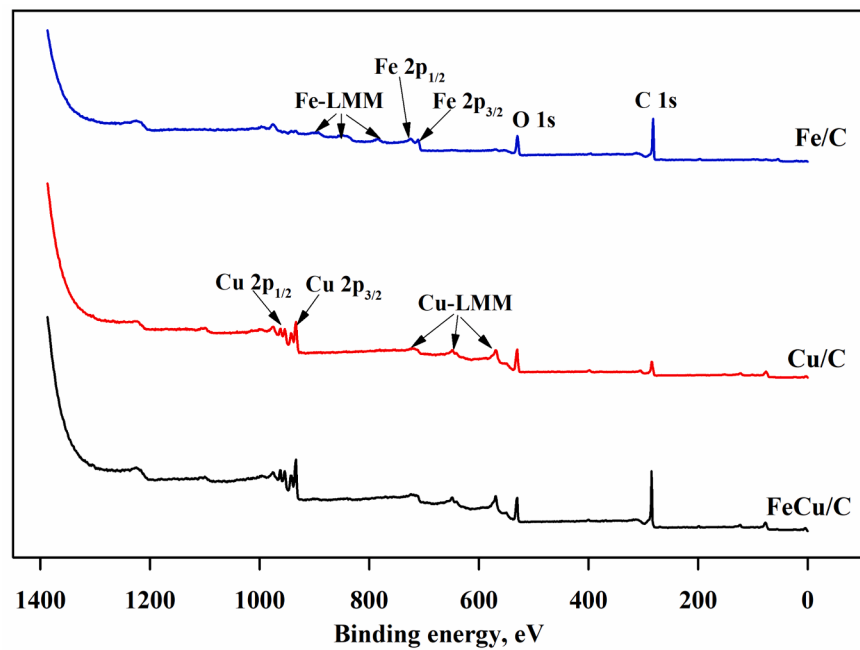


Fig. 3. XPS spectra of three synthesized catalysts.

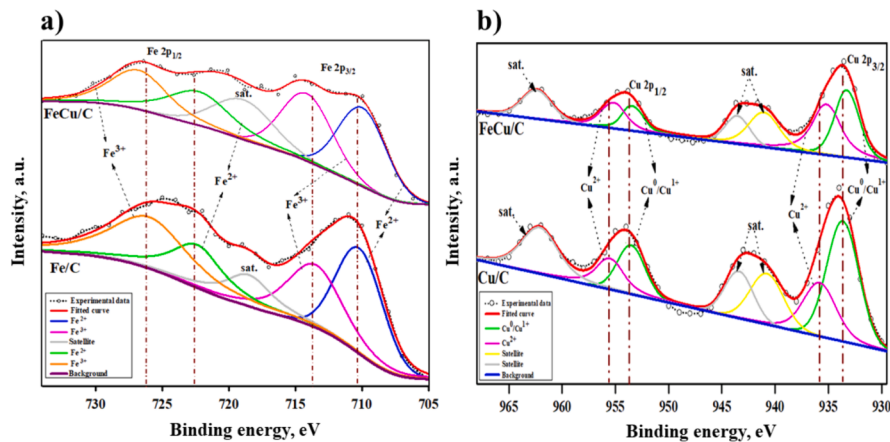


Fig. 4. a) Fe 2p deconvolution of XPS spectra of Fe/C and Fe,Cu/C catalysts, b) Cu 2p deconvolution of XPS spectra of Cu/C and Fe,Cu/C catalysts.

that Fe and Cu metals are not included in each other's crystal structures and that the two metals do not form alloys. Additionally, to identify the presence of oxidized iron species in the Fe/C structure, an enlargement of the XRD pattern of FeCu/C is given in Fig. S1.

SEM images taken at different magnifications and EDS analysis results for Fe/C, Cu/C, and Fe,Cu/C catalysts are shown in Fig. 2. The micrographs illustrate the morphology of the catalyst material, with the bright parts providing information on the presence of metal particles. Metal clusters are observed in some sections of the images. The EDS data for the synthesized catalysts confirm that their structures include Fe, Cu, and C elements. EDS analysis of Fe,Cu/C catalysts shows an equal distribution of Fe and Cu, in agreement with the EDS results of Fe/C and Cu/C catalysts.

XPS analysis was performed to determine the binding configurations, surface composition, and chemical states of the elements in the structure of the catalysts, Fig. 3. C, O, Fe, and Cu elements were observed in the XPS scanning spectra of the catalysts. The peaks at approximately 952.3 and 932.15 eV binding energies correspond to Cu 2p [32], at 718.46, 6447.98, and 567.25 eV to Cu LMM (LMM Auger transitions of pure Cu) [32], at 897.32, 848.87, and 786.15 eV to Fe 2p [33], at 724.8 and

710.8 eV to Fe-LMM (LMM Auger transitions of pure Fe) [33], at 532 eV to O 1s, and at 284 eV to C 1s [34]. The observed peaks were compatible with the prepared catalyst structure and the literature data. The peaks of both Fe and Cu elements in the Fe,Cu/C catalyst indicate that these metals are successfully loaded into the carbon material. In addition, the presence of the O peak is observed for all catalysts due to the physical adsorption of oxygen during the analysis [35,36].

High-resolution Fe 2p spectra of Fe/C and FeCu/C reveal two characteristic peaks centered at binding energies of 710.5 and 723.4 eV attributed to Fe 2p_{3/2} and 2p_{1/2}, respectively, Fig. 4a. After deconvolution, peaks at 710.6 and 723.3 eV are indexed to Fe²⁺, while peaks at 713.5 eV and 725.9 eV are attributed to Fe³⁺. The additional peak at 718.8 eV is attributed to the shaking of the satellite [37,38].

Similarly, the peaks seen at 933.8 and 953.7 eV in the Cu 2p spectra of Cu/C and FeCu/C are attributed to Cu 2p_{3/2} and Cu 2p_{1/2}, respectively, with two satellite peaks at 943.7 and 963.1 eV, Fig. 4b. When this Cu 2p_{3/2} signal is deconvoluted, two peaks at 933.2 and 934.8 eV can be attributed to (Cu⁰/Cu¹⁺) and Cu²⁺, respectively. In a similar vein, Cu 2p_{1/2} signal is deconvoluted into two peaks at 953.5 and 955.8 eV attributed to (Cu⁰/Cu¹⁺) and Cu²⁺ [39]. Thus, the peaks in the Fe/C,

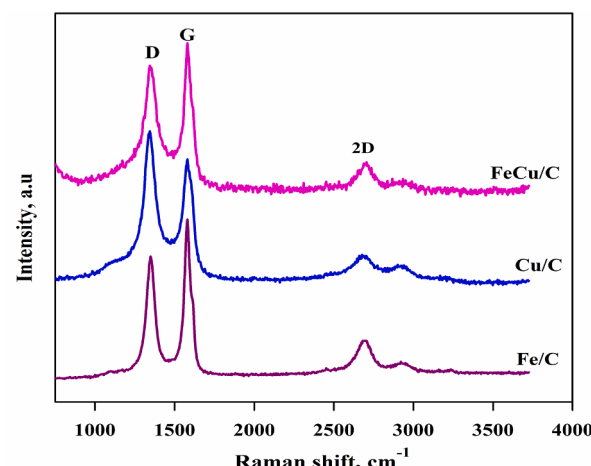


Fig. 5. Raman spectra of three synthesized catalysts.

Cu/C, and FeCu/C spectra are compatible with the composition of the synthesized catalysts, and the binding energy values are the same or very close to the values reported in the literature [40]. When the Fe 2p

spectra of Fe/C (Fig. 4a) and Cu 2p spectra of Cu/C (Fig. 4b) are compared with the FeCu/C catalyst, the peaks in the structure of the bimetallic catalyst are consistent with the monometallic-based structure. Moreover, it has been determined that the peaks of the Fe,Cu/C catalyst shift slightly compared to the monometallic-based structure possibly due to the electron interaction between the two metals. While these shifts due to the interaction between metal atoms are towards higher binding energies in Fig. 4a, they are towards lower binding energies in Fig. 4b. Moreover, the high resolution Cu 2p (Fig. 4a) and Fe 2p XPS (Fig. 4b) spectra of the FeCu/C catalyst revealed that both Cu and Fe elements have multiple valences, including Cu^0 , Cu^{1+} , and Cu^{2+} in case of Cu and Fe^{2+} and Fe^{3+} in case of Fe. These metal valences are consistent with the peaks observed in the FeC/C catalyst's XRD pattern. Additionally, Fig. S2 also provides high-resolution C1s and O1s partial XPS spectra of the synthesized catalysts. The C1s spectra, divided into four peaks, depict the chemical bonding state of the carbon in the structure (Fig. S2a, c, e). When the C1s peak is decomposed into sub-peaks, peat at 283.2 eV corresponds to the $\text{C}=\text{C}$ bond, 284.4 eV to the $\text{C}-\text{C}$ bond, 285.8 eV to the $\text{C}-\text{O}$ bond, and 287.2 eV to the $\text{C}=\text{O}$ bond. The $\text{C}=\text{C}$ bond is the bonding pattern of carbon atoms undergoing sp^2 hybridization and represents proximity to the graphitic structure, while the others most likely indicate impurities in graphite. As the sp^2/sp^3 ratio increases, graphite-like properties become dominant, while

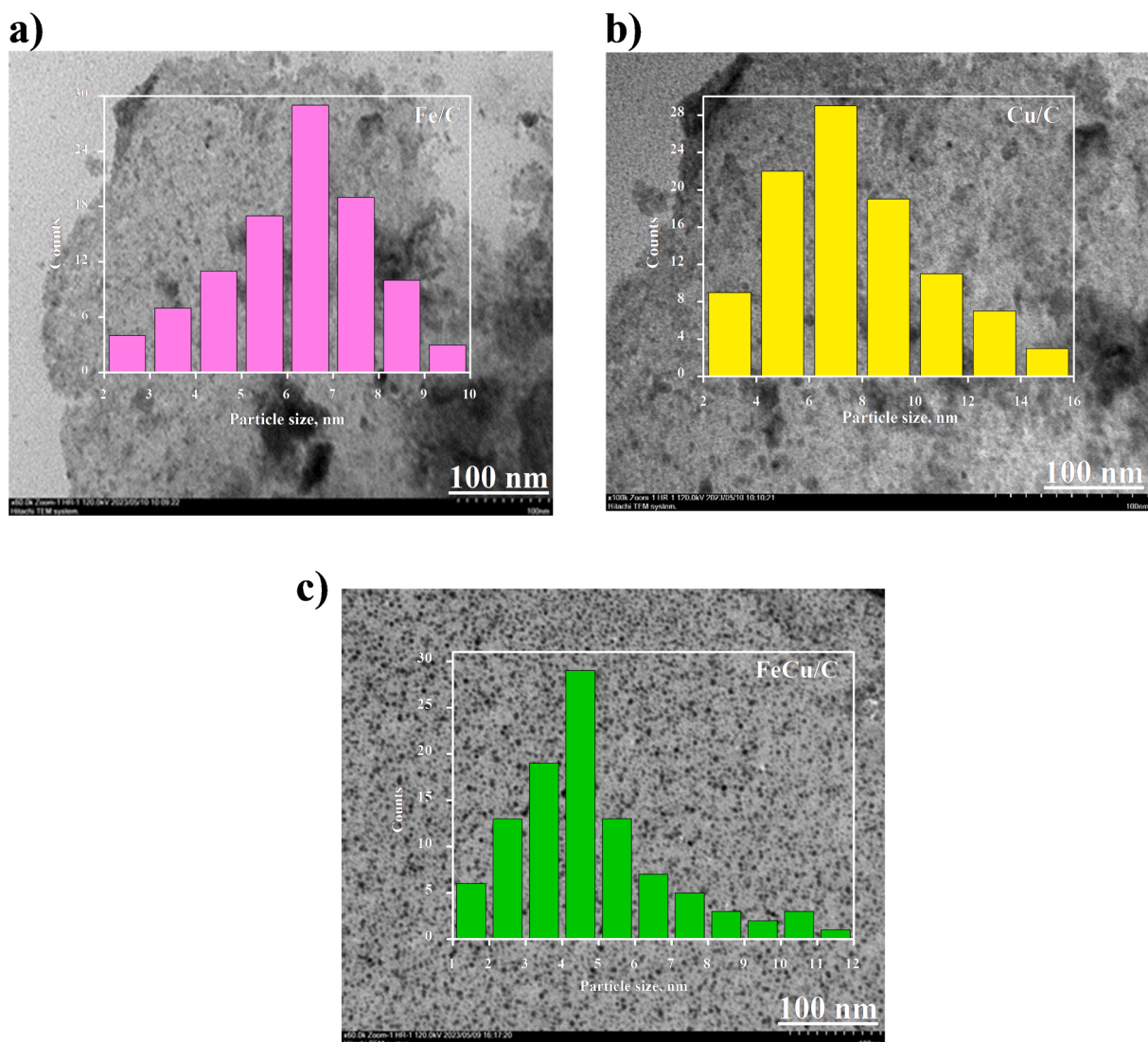


Fig. 6. TEM images of synthesized (a) Fe/C, (b) Cu/C, and (c) Fe,Cu/C catalysts and the corresponding particle size distribution histograms.

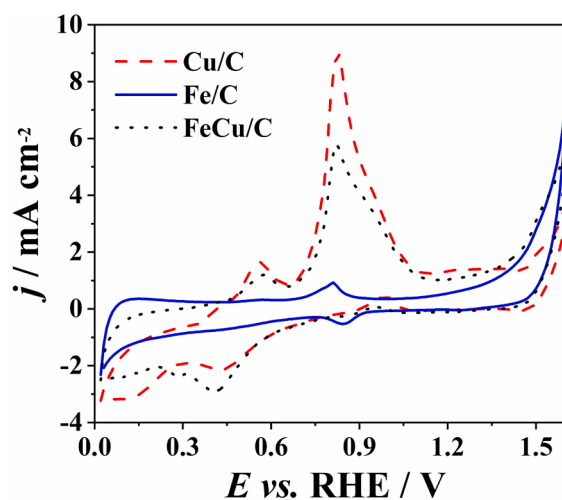


Fig. 7. CVs of Fe/C, Cu/C, and Fe,Cu/C in 8 M KOH at 25 mV s⁻¹ and 25 °C.

diamond-like properties become dominant when the ratio decreases. In particular, the Fe/C catalyst has the highest sp²/sp³ ratio, indicating that this sample has higher graphite properties than the other samples. Fig. S2b, d, f shows the high-resolution O 1 s spectrum, which can be decomposed into four peaks at 528.4, 530.5, 532.8, and 533.7 eV, respectively. The peak at the binding energy of 528.4 eV corresponds to the metal–oxygen (M–O) lattice. This peak confirms the formation of the Fe–O structure on a Fe-based catalyst and the Cu–O structure on a Cu-based catalyst. Thus, the metal–O bond's presence is consistent with the XRD analysis's findings. The other sub-peaks represent O bonding with element C and adsorbed oxygen.

Another analysis used to examine the structural changes, defects and irregularities in the structure, of synthesized carbon-based catalysts was Raman spectroscopy, Fig. 5. The Raman spectra of all catalysts are quite similar and two distinct peaks belonging to the D and G bands can be seen at 1341 cm⁻¹ and 1578 cm⁻¹, respectively [41]. In addition, the characteristic peak around 2700 cm⁻¹ is defined as the 2D band. The D band shows the irregularity in the structure, and the G band shows the degree of graphitization in relation to sp² hybridization [42,43]. The degree of graphitization has an important effect on the conductivity performance of carbon-based materials. Accordingly, the ratio of the D band and G band peak intensities, I_D/I_G , is examined to detect the structural irregularity of the carbon material [44]. The I_D/I_G ratios of t Fe/C, Cu/C, and Fe,Cu/C are 0.88, 1.08, and 0.97, respectively. Cu/C has the highest degree of defective graphitization, i.e., it has an irregular structure and more defects than the others. Obviously, the I_D/I_G ratio of the Fe,Cu/C sample shows that a balance has started to occur between defective sites and graphitization [41]. Additionally, based on the spectra depicted in Fig. S2a, c, e it is evident that Fe/C exhibits the highest sp²/sp³ ratio, i.e., it has a more pronounced graphite structural characteristic. The XPS findings were thus corroborated by the data derived from Raman analysis (the lowest I_D/I_G ratio in case of Fe/C).

TEM images of synthesized catalysts are given in Fig. 6. The dark, highly dispersed, spherical-like particles in the images indicate the presence of metal particles on the carbon. The particle of the bimetallic Fe,Cu/C catalyst have a more distinct shape than the others and showed a homogeneous distribution. It is seen that there are agglomerations in some parts of the monometallic catalysts. In addition, histograms representing the particle size distributions are shown over the TEM images. The approximate particle sizes determined for Fe/C, Cu/C, and Fe,Cu/C catalysts were 7.21 nm, 6.68 nm, and 4.80 nm, respectively. In previous studies, Fe,Cu particle of 4 to 10 nm size were reported [33,34]. The Fe, Cu particle sizes obtained in this study also fall within this specified range.

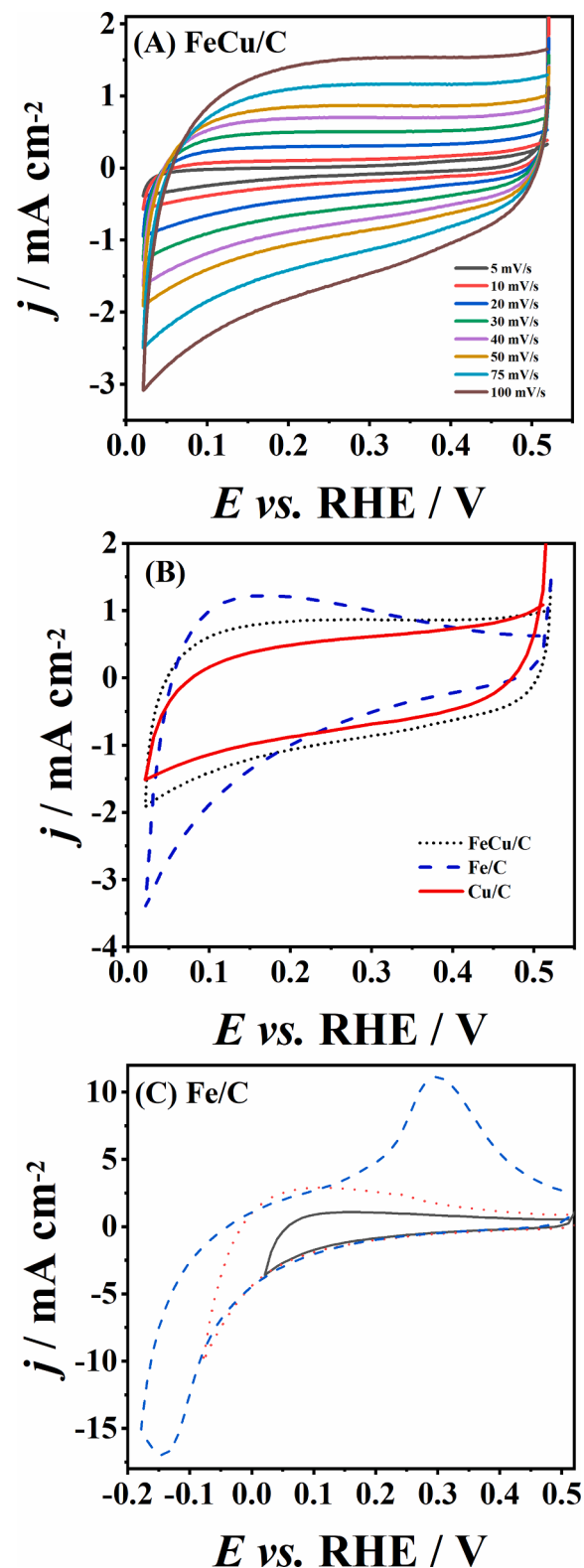


Fig. 8. Cyclic voltammograms of (A) Fe,Cu/C at different scan rates and (B) Fe/C, Cu/C and Fe,Cu/C catalysts at 50 mV s⁻¹ in 0.0–0.5 V range, and of (C) Fe/C at 50 mV s⁻¹ with different cathodic cut-off potentials in 8 M KOH.

3.2. Electrochemical characterization: double-layer capacitance and hydrogen bonding

The redox behaviour of the three materials was scrutinized by cyclic voltammetry in 8 M KOH, with the CV curves shown in Fig. 7. CV of Fe/C

Table 1

Specific capacitance values for Fe/C, Cu/C, and Fe,Cu/C at different scan rates.

| Electrocatalyst | Scan rate/mVs ⁻¹ | | | | | | | |
|-----------------|-------------------------------|-------|-------|-------|-------|-------|-------|-------|
| | 5 | 10 | 20 | 30 | 40 | 50 | 75 | 100 |
| | Capacitance/F g ⁻¹ | | | | | | | |
| Fe/C | 25.81 | 25.13 | 20.29 | 19.12 | 19.12 | 17.58 | 16.48 | 16.13 |
| Cu/C | 18.13 | 14.08 | 10.34 | 9.38 | 8.72 | 9.71 | 8.08 | 8.21 |
| Fe,Cu/C | 20.62 | 17.76 | 16.96 | 16.96 | 16.92 | 16.36 | 14.24 | 13.67 |

displays a pair of redox peaks in 0.81–0.85 V region due to the presence of Fe(II)/Fe(III) redox couple, *i.e.*, oxidation to and subsequent reduction of Fe(III) species such as Fe_2O_3 , FeOOH , and Fe_3O_4 [47,48]. On the other hand, peaks at 0.56 and 0.82 V at CVs of Cu/C and Fe,Cu/C can be attributed to the oxidation of Cu to Cu(I) and then Cu(II) species [49], or oxidation to Cu_2O and then $\text{Cu}(\text{OH})_2$ [50].

Additional voltammetry studies were performed to elucidate the charge storage capability of the three electrocatalysts in alkaline media. The charge storage behavior of three catalysts was initially investigated within the 0–0.5 V potential region. Fig. 8A illustrates the case of Fe,Cu/C; a steady capacitance performance is evidenced by no change in shape of cyclic voltammograms with changing the sweep rate. The specific capacitance C_s of the three electrocatalysts decreased when the sweep rate increased (Table 1), most likely due to the restricted capability of electrolyte ions to enter into the materials' pores at higher sweep rates [51]. Comparing the CVs of three electrocatalysts shows that Fe/C possesses somewhat higher specific capacitance (Fig. 8B and Table 1), most likely due to the higher surface porosity (Fig. 2a,c,e).

Electrochemical active surface area (ECSA) of three materials was next assessed. Cyclic voltammetry was run close to the open circuit potential, *i.e.*, in non-faradaic region, to determine the double-layer capacitance, C_{dl} , Fig. S3. The highest C_{dl} value of $0.44 \mu\text{F cm}^{-2}$ was obtained for Fe/C, followed by values of 0.28 and $0.26 \mu\text{F cm}^{-2}$ for Cu/C and Fe,Cu/C, respectively. These C_{dl} values of the same order of magnitude correspond to ECSAs of three catalysts of the same order of magnitude.

3.3. Oxygen evolution reaction study

As OER limits the efficiency of water electrolysis process, the three catalysts' performance for this reaction was first assessed [52]. Fig. 9A presents the polarization curves of the three studied electrocatalysts in 8 M KOH (concentration typically used in industrial alkaline water electrolyzers). It can be seen that Fe,Cu/C delivers the highest current density during OER, followed by Fe/C, and finally, Cu/C. OER starts notably earlier (ca. 200 mV) at Fe,Cu/C (onset potential, $E_{onset} = 1.319$ V) compared to Fe/C ($E_{onset} = 1.536$ V) and Cu/C ($E_{onset} = 1.572$ V). The overpotential for reaching 10 mA cm^{-2} , η_{10} , has the lowest value for Fe, Cu/C (325 mV) among the three materials; values of 417 and 505 mV were observed for Fe/C and Cu/C, respectively (Table 2). Furthermore, η_{10} value of Fe,Cu/C is lower than in case of number of Fe- and Cu-based electrocatalysts reported in the literature including NiFeC (345 mV), Fe-NiP (342 mV), FeNiS (370 mV), FeCo (375 mV), $\text{Cu}_{0.08}\text{Co}_{0.92}\text{PNAs/CP}$ (411 mV) and $\text{Cu}_3\text{P}/\text{CF}$ (610 mV) or comparable as in case of $\text{Cu}_2\text{S}-\text{Ni}_3\text{S}_2/\text{NF}$ (329 mV) (Table 2), suggesting lower energy barrier and faster OER kinetics at the herein introduced electrocatalyst. This trend of Fe, Cu/C demonstrating the favourable OER is also evident when determining the current density at 400 mV of overpotential. Fe,Cu/C delivered the highest j_{400} of ca. 83.8 mA cm^{-2} , with this value being more than 5 and 21 times higher than j_{400} of Fe/C and Cu/C, respectively. High activity of Fe,Cu-based electrocatalysts towards OER has been previously reported [53]. Namely, CuFe_2O_4 nanofibers electrocatalysts showed higher OER performance with lower charge-transfer resistance, R_{ct} , overpotential and Tafel slope compared to NiFe_2O_4 , MnFe_2O_4 and Fe_2O_3 nanofibers in alkaline medium [53]. It is worth

noting that current density at 1.65 V recorded using Fe,Cu/C was more than $30\times$ higher than that of CuFe_2O_4 nanofibers.

Tafel analysis of OER polarization curves (Fig. 9B) revealed Tafel slope, b , value of $163.5 \text{ mV dec}^{-1}$ for Fe,Cu/C, while higher b values of 168.3 and $184.5 \text{ mV dec}^{-1}$ were determined for Cu/C and Fe/C, respectively (Fig. 9B). OER Tafel slope values typically fall within the 30 to 120 mV dec^{-1} range [54,55] depending on the exact mechanism and the rate-determining step (Eqs. (3)–(7)) [56]. Complex mechanism of OER involves transfer of four electrons within subsequent steps, including the interaction of OH^- with the electrocatalyst's surface. Adsorbed OH^- undergoes 1e^- oxidation to MOH (Eq. (3)), followed conversion of MOH to MO upon elimination of 1 proton and 1 electron (Eq. (4)). Two MO can directly recombine, producing O_2 (Eq. (5)) and liberating two active centers. Optionally, MO can convert to M-OOH by merging with OH^- ion through 1e^- oxidation (Eq. (6)), with subsequent proton-coupled electron transfer generating O_2 and liberating one active center (Eq. (7)) [56].

The OER Tafel slope value evaluated for Fe,Cu/C is higher than the expected range. Still, it should be kept in mind that experimental conditions (scan rate, for example) and data treatment (IR-compensation percentage) can have a significant impact on the OER kinetic parameters [57] and therefore, it is crucial to account for variations in experimental setups and data analysis methods when comparing Tafel slope values reported in the literature (Table 2).



Fig. 9C shows the Nyquist plots of Fe/C, Cu/C, and Fe,Cu/C, with the equivalent circuit (inset) used to determine the EIS parameters. The low charge-transfer resistance, R_{ct} , was evaluated for Fe/C and FeCu/C (Table S1), explaining their higher OER current density obtained by the LSV method than in case of Cu/C. Introducing Fe into different catalytic systems was demonstrated to be beneficial and vital for notable enhancement of their catalytic activity towards OER. For instance, presence of Fe^{3+} ions was reported to alter the nature of Co^{2+} active centers via electronic interaction and geometrical confinement that further restrain the multipath reversible phase conversion of cobalt oxides during OER [58]. The existence of Fe in Cu-based electrocatalyst could enhance its performance and catalysis of OER by increasing the number of covalent bonds in metal-ion bonds [59]. Also, coexistence of copper oxide and iron oxide was demonstrated to be beneficial for catalysis of OER in alkaline media [60]. The number of active OER sites of Fe was controlled by the strong interaction of Fe with the host [52,61,62].

3.4. Hydrogen evolution reaction study

Polarization curves for the three studied electrocatalysts were also recorded under cathodic (HER) polarization conditions in 8 M KOH, Fig. 10A. Onset potential was found to be ca. 27 and 45 mV less negative

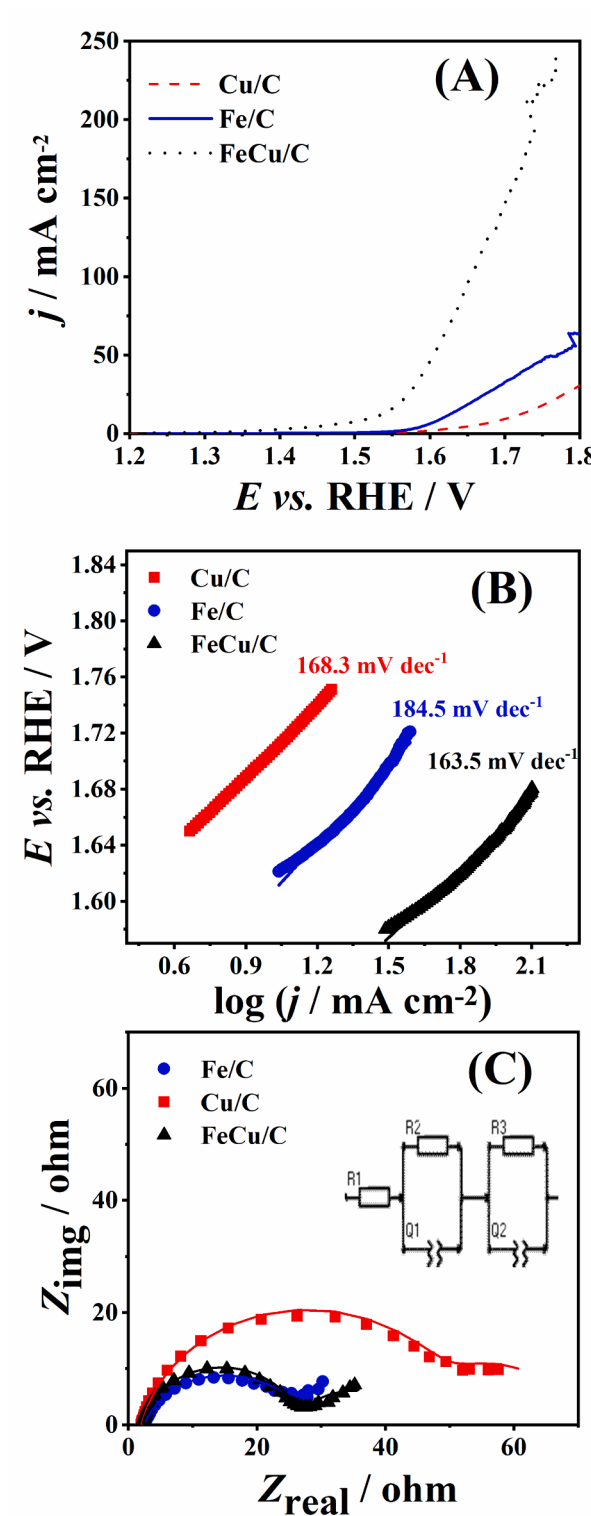


Fig. 9. OER polarization curves for Fe/C, Fe,Cu/C, and Cu/C (A) and the corresponding Tafel plots (B). Nyquist plots of three electrocatalysts at 1.8 V with the corresponding equivalent circuit in the inset (C). All measurements are done in 8 M KOH at 25 °C.

for Fe/C (-0.308 V) and Cu/C (-0.290 V), respectively, compared to bimetallic Fe,Cu/C (-0.335 V) (Table 3 and Table S2). Accordingly, current densities at Fe/C and Cu/C were somewhat higher than those at bimetallic Fe,Cu/C. Tafel analysis of polarization curves at 25 °C (Fig. 10B) revealed b values of 132, 155, and 152 mV dec^{-1} for Fe/C,

Table 2

Comparison of the performance for OER in alkaline medium of herein studied and literature-reported Fe- and Cu-based electrocatalysts.

| Electrocatalyst | Electrolyte | $E_{\text{onset}}/\text{V}$ | $b/\text{mV dec}^{-1}$ | η_{10}/mV | $j_{400}/\text{mA cm}^{-2}$ | Source |
|--|-------------|-----------------------------|------------------------|-----------------------|-----------------------------|-----------|
| Fe/C | 8 M KOH | 1.536 | 184.5 | 417 | 15.8 | This work |
| Cu/C | 8 M KOH | 1.572 | 168.3 | 505 | 4.0 | This work |
| Fe,Cu/C | 8 M KOH | 1.319 | 163.5 | 325 | 83.8 | This work |
| NiFeCMo-30 | 30 % KOH | 60.3 | 256 | | | [63] |
| NiFeC | 30 % KOH | 81.8 | 345 | | | [63] |
| NiFeCMo-20 | 30 % KOH | 65.6 | 279 | | | [63] |
| NiFeCMo-40 | 30 % KOH | 70.5 | 269 | | | [63] |
| Fe-NiPPv) | 1 M KOH | 41.15 | 290 | | | [64] |
| Fe-NiP | 1 M KOH | 94.88 | 342 | | | [64] |
| Ni-NCN/CoFe-LDH | 1 M KOH | 42.87 | 280 | | | [65] |
| FeNiS | 1 M KOH | 80 | 370 | | | [66] |
| FeNiS-MWCNT | 1 M KOH | 50 | 260 | | | [66] |
| FeCo | 1 M KOH | 119.39 | 375 | | | [67] |
| Ru/FeCo | 1 M KOH | 79.08 | 283 | | | [67] |
| Fe/NF | 1 M KOH | 79.71 | 236 | | | [68] |
| $\text{Cu}_{0.08}\text{Co}_{0.92}\text{PNAs/CP}$ | 1 M KOH | 101.4 | 411 | | | [69] |
| $\text{Cu}_3\text{P/CF}$ | 1 M KOH | 208 | 610 | | | [69] |
| $\text{Cu}_{2.5}\text{S-Ni}_3\text{S}_2/\text{NF}$ | 1 M KOH | 44.11 | 329 | | | [70] |
| $\text{Cu}_{0.5}\text{Fe}_{0.5}/\text{NF}$ | 1 M KOH | 62.07 | 218 | | | [68] |
| Cu/NF | 1 M KOH | 155.23 | 252 | | | [68] |
| $\text{CuFe}_2\text{O}_4 \text{ NF}^*$ | 0.1 M KOH | 1.64 | 93.97 | | | [53] |
| $\text{CuFe}_2\text{O}_4 \text{ NP}$ | 0.1 M KOH | 1.71 | 237.32 | | | [53] |

P_v – phosphorus vacancies; LDH – layered double hydroxide; MWCNT – multi-walled carbon nanotube; NA – nanosheet array; CP – carbon paper; CF – copper foam; NF – nickel foam; NF* – nanofiber; NP – nanoparticles.

Cu/C, and Fe,Cu/C, respectively (Table 3 and Table S2). These values further indicate the HER mechanism. Complex mechanism of HER, either Volmer-Heyrovský or Volmer-Tafel, involves two electrochemical steps or an electrochemical step followed by a chemical step [71]. Electrochemical hydrogen adsorption on the electrocatalyst, MH_{ads} , (Eq. (8)) precedes electrochemical desorption (Eq. (9)) or catalytic recombination (Eq. (10)).



Tafel slope values of 120, 40, and 30 mV dec^{-1} suggest Volmer, Heyrovský, and Tafel stages, respectively, determining the process rate. A b of 120 mV dec^{-1} is also reported for the Heyrovský step governing the kinetics when a high coverage of adsorbed hydrogen (>0.6) is observed [54]. The herein-determined Tafel slope values at 25 °C indicate HER proceeding via Volmer-Heyrovský pathway. Also, with increasing temperature, the Tafel slope of HER at Fe/C decreased, indicating faster reaction kinetics at higher temperatures, but the reaction mechanism remained unchanged. As for Cu/C and Fe,Cu/C, Tafel slope did not decrease with temperature, possibly due to the slow diffusion of the evolved H₂ gas from the active sites and consequent partial blocking of the electrode surface by the bubbles.

Continuing capacitance studies described above by extending the potential window below 0 V as the thermodynamic potential value of HER (Fig. 8C), the reduction current corresponding to the evolution of hydrogen was recorded. The hydrogen oxidation peak is shifted towards a more positive value compared to the thermodynamic one, suggesting that the binding of adsorbed hydrogen is stronger than ideal (i.e., right side of the volcano plot). This might further result in a higher

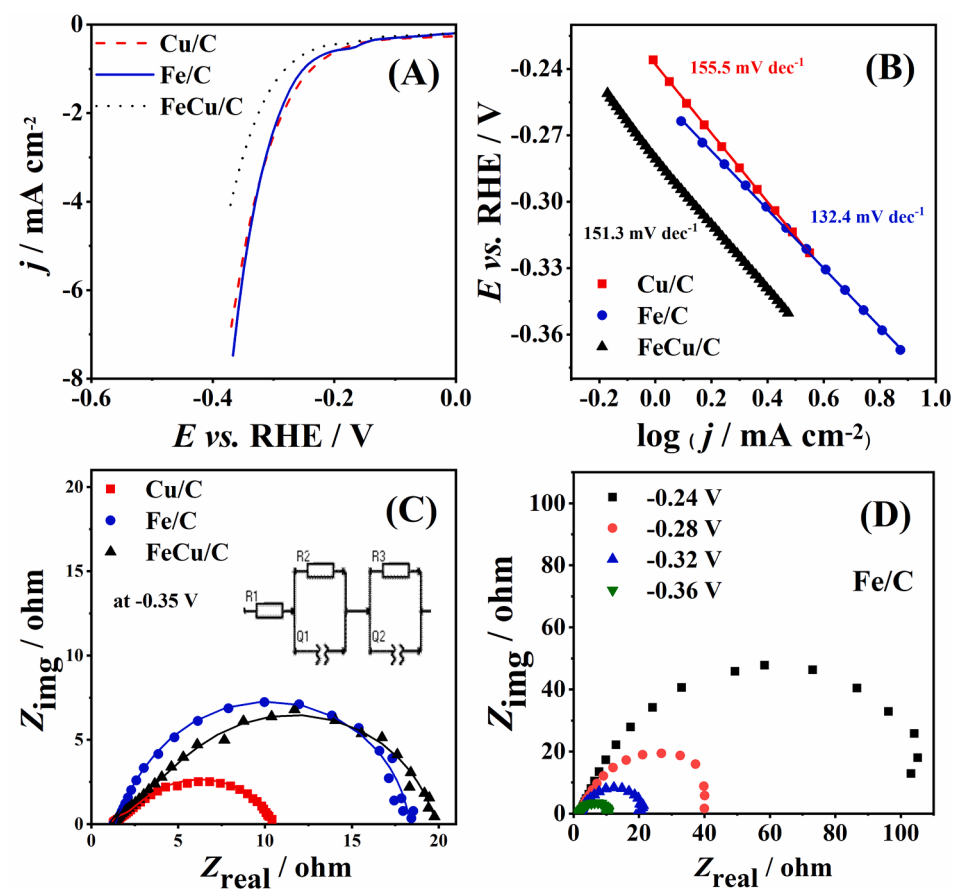


Fig. 10. HER polarization curves of Fe/C, Cu/C and Fe,Cu/C (A) and corresponding Tafel plots (B); Nyquist plots of the three electrocatalysts with the corresponding equivalent circuit in the inset (C); Nyquist plots of Fe/C at different potentials (D). All measurements are done in 8 M KOH at 25 °C.

Table 3

Comparison of parameters of HER in alkaline medium at herein studied and literature-reported Fe- and Cu-based electrocatalysts.

| Electrocatalyst | Electrolyte | $E_{\text{onset}} / \text{V}$ | $b / \text{mV dec}^{-1}$ | η_{10} / mV | Source |
|---|-------------|-------------------------------|--------------------------|-------------------------|-----------|
| Fe/C | 8 M KOH | -0.308 | 132 | — | This work |
| Cu/C | 8 M KOH | -0.290 | 152 | — | This work |
| Fe,Cu/C | 8 M KOH | -0.335 | 150 | — | This work |
| NiFeCMo-30 | 30 % KOH | 163.9 | 254 | [63] | |
| NiFeC | 30 % KOH | 134.9 | 381 | [63] | |
| NiFeCMo-20 | 30 % KOH | 123.4 | 290 | [63] | |
| NiFeCMo-40 | 30 % KOH | 134.2 | 300 | [63] | |
| Co-FeP/3D rGO | 1 M KOH | 77.4 | 188 | [74] | |
| FeCo | 1 M KOH | 88.4 | 361 | [67] | |
| Ru/FeCo | 1 M KOH | 82.8 | 155 | [67] | |
| FeNF | 1 M KOH | 75.5 | 162 | [68] | |
| $\text{Cu}_{0.08}\text{Co}_{0.92}\text{P}$ NAs/CP | 1 M KOH | 83.5 | 81 | [69] | |
| $\text{Cu}_2\text{P}/\text{CF}$ | 1 M KOH | 167.9 | 239 | [69] | |
| $\text{Cu}_2\text{S}-\text{Ni}_3\text{S}_2/\text{NF}$ | 1 M KOH | 75.9 | 149 | [70] | |
| $\text{Cu}_{0.5}\text{Fe}_{0.5}/\text{NF}$ | 1 M KOH | 62.2 | 158 | [68] | |
| Cu/NF | 1 M KOH | 103.8 | 164 | [68] | |

rGO – reduced graphene oxide; NA – nanosheet array; CP – carbon paper; NF – Ni foam.

overpotential required for driving HER and higher than expected Tafel slope values observed herein [51]. Previous studies involving polycrystalline Cu that underwent different pretreatments revealed more than 4 orders of magnitude difference in their activity, assigned to the

different degree of surface oxidation [72]. It was demonstrated that surface of higher degree of oxidation where Cu(I) species is dominant over Cu(0) encompasses higher amount of adsorbed oxygen species (namely, O and OH), and thus turn more hydrophilic adsorbing water more strongly. Thus, existence of activated M-OH_{ad}–OH₂ complex is vital for lowering the energy barrier for water molecule splitting [73].

EIS measurements with three electrocatalysts under HER conditions showed R_{ct} values of the same order of magnitude, Fig. 10C. For Fe/C, which gave the highest current densities and the lowest Tafel slope, measurements were made at different negative potentials (Fig. 10D) and temperatures (Fig. S4D). A considerable dependence of R_{ct} of Fe/C on the working potential is observed, Fig. 10D. The more negative the value of the working potential, the lower the charge-transfer resistance (a decrease from ca. 100 Ω at -0.24 V to ca. 10 Ω at -0.36 V, Table S3), and thus more efficient the HER. Fig. S4D shows the Nyquist plots at different temperatures, from 25 °C to 85 °C, where it can be seen that the temperature increment did not affect the R_{ct} at the solid/electrolyte interface.

3.5. Stability study

Finally, the stability of materials performance under OER and HER conditions was probed, Fig. 11. One of the challenges related to the use of IL-derived transition metal-based electrocatalysts is sustaining their performance in a harsh chemical environment of water electrolysis over long period [22]. Herein investigated electrocatalysts demonstrated satisfactory stability. Namely, anodic (OER) current density of Fe,Cu/C was constant during 24 h. Fe-active species were previously observed to be dynamically stable because of dissolution and redeposition at the contact surface between the electrolyte and electrocatalysts interface

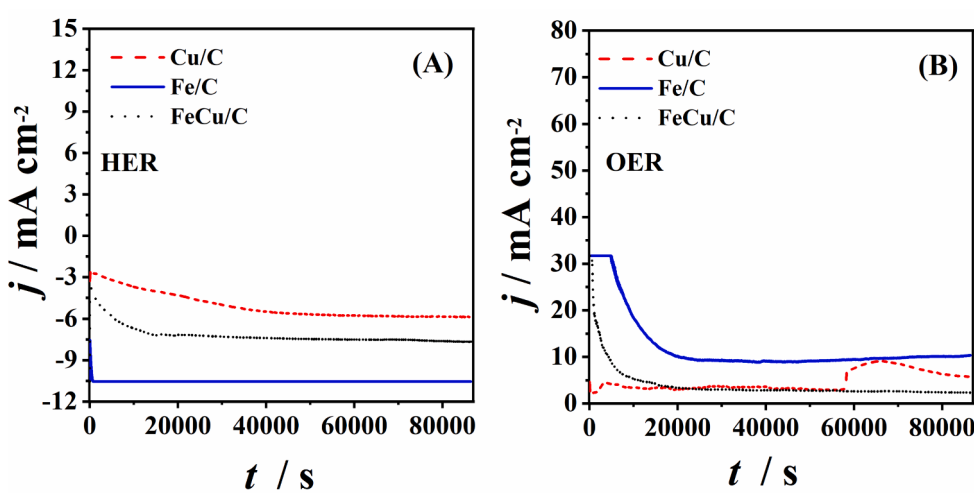


Fig. 11. Chronoamperometric curves of studied electrocatalysts under HER (-0.35 V) and OER (1.8 V) polarisation.

[52,61,62]. OER current density of Fe/C decreased in the first 4 h, and then slightly increased with time, while Cu/C gave constant OER current density in the first 16 h, and then somewhat increased up to about 21 h and again decreased up to the end of the chronoamperometric test of stability.

Chronoamperometric measurements revealed the highest current density in the case of Fe/C for HER, in agreement with the voltammetric data. Moreover, the cathodic (HER) current density of Fe/C remained unchanged throughout the measurement (24 h). Similar behavior of FeCu/C electrocatalyst was obtained, while Cu/C showed a less stable HER current density during the chronoamperometric test of stability.

4. Conclusions

In this work, carbon materials decorated with Fe-, Cu, and with Fe and Cu (Fe/C, Cu/C, and Fe,Cu/C) were produced by direct carbonization of Fe- or/and Cu-containing ionic liquids. They were scrutinized for oxygen and hydrogen evolution reactions in alkaline electrolyte. Fe/C and FeCu/C electrocatalysts provide low charge-transfer resistance under the OER polarization conditions. This led to a low OER onset potential accompanied by a high current density, especially in the case of Fe,Cu/C that reached 10 mA cm⁻¹ at 325 mV of overpotential. In addition, the synthesized materials demonstrate good long-term stability under both anodic and cathodic polarization condition. Thus, herein examined Fe- and Cu-decorated carbon, particularly Fe,Cu/C, show promising performance as electrocatalysts for efficient production of oxygen and hydrogen by alkaline water splitting.

CRediT authorship contribution statement

Jelena Georgijević: Writing – original draft, Visualization, Investigation, Formal analysis. **Jadranka Milikić:** Visualization, Investigation, Formal analysis, Writing – original draft. **Yasemin Aykut:** Writing – original draft, Investigation, Formal analysis. **Nikola Zdolšek:** Writing – original draft, Investigation, Conceptualization. **Diogo M.F. Santos:** Writing – review & editing, Conceptualization. **Ayşe Bayrakçeken:** Writing – review & editing, Supervision, Formal analysis. **Biljana Šljukić:** Writing – review & editing, Supervision, Conceptualization.

Declaration of competing interest

The authors declare that they have no known competing financial interests or personal relationships that could have appeared to influence the work reported in this paper.

Acknowledgments

The authors would like to thank the Ministry of Science, Technological Development and Innovation of the Republic of Serbia (contract nos. 451-03-65/2024-03/200146, 451-03-66/2024-03/200146 and 451-03-66/2024-03/200017). The authors would also like to thank Fundação para a Ciéncia e a Tecnologia (FCT, Portugal) for contract IST-ID/156/2018 (B. Šljukić) and a contract in the scope of programmatic funding UIDP/04540/2020 (D.M.F. Santos).

Appendix A. Supplementary data

Supplementary data to this article can be found online at <https://doi.org/10.1016/j.jelechem.2024.118455>.

References

- [1] L. Zhang, H. Zhao, S. Xu, Q. Liu, T. Li, Y. Luo, S. Gao, X. Shi, A.M. Asiri, X. Sun, Recent advances in 1D electrospun nanocatalysts for electrochemical water splitting, *Small Struct.* 2 (2021) 2000048, <https://doi.org/10.1002/sstr.202000048>.
- [2] M.-H. Chung, J.Y. Ro, The medical uses of hydrogen, *Food Suppl. Biomater. Heal.* 1 (2021), <https://doi.org/10.5236/fshb.2021.1.e5>.
- [3] L. Li, P. Wang, Q. Shao, X. Huang, Metallic nanostructures with low dimensionality for electrochemical water splitting, *Chem. Soc. Rev.* 49 (2020) 3072–3106, <https://doi.org/10.1039/d0cs00013b>.
- [4] J. Wang, W. Cui, Q. Liu, Z. Xing, A.M. Asiri, X. Sun, Recent progress in cobalt-based heterogeneous catalysts for electrochemical water splitting, *Adv. Mater.* 28 (2016) 215–230, <https://doi.org/10.1002/adma.201502696>.
- [5] G. Liu, Y. Xu, T. Yang, L. Jiang, Recent advances in electrocatalysts for seawater splitting, *Nano Mater. Sci.* 5 (2023) 101–116, <https://doi.org/10.1016/j.nanoms.2020.12.003>.
- [6] S. Anantharaj, S. Noda, Amorphous catalysts and electrochemical water splitting: an untold story of harmony, *Small* 16 (2020), <https://doi.org/10.1002/smll.201905779>.
- [7] S. Wang, A. Lu, C.J. Zhong, Hydrogen production from water electrolysis: role of catalysts, *Nano Converg.* 8 (2021), <https://doi.org/10.1186/s40580-021-00254-x>.
- [8] J. Wang, X. Yue, Y. Yang, S. Sirisomboonchai, P. Wang, X. Ma, A. Abudula, G. Guan, Earth-abundant transition-metal-based bifunctional catalysts for overall electrochemical water splitting: A review, *J. Alloys Compd.* 819 (2020), <https://doi.org/10.1016/j.jallcom.2019.153346>.
- [9] Q. Li, Y. Gao, M. Liu, W. Xiao, G. Xu, Z. Li, F. Liu, L. Wang, Z. Wu, Ultrafast synthesis of halogen-doped Ru-based electrocatalysts with electronic regulation for hydrogen generation in acidic and alkaline media, *J. Colloid Interface Sci.* 646 (2023) 391–398, <https://doi.org/10.1016/j.jcis.2023.05.065>.
- [10] Advanced Materials - 2023 - Wu - Microwave Phosphine-Plasma-Assisted Ultrafast Synthesis of Halogen-Doped Ru RuP2 with.pdf, (n.d.).
- [11] S. Anantharaj, S. Kundu, Do the evaluation parameters reflect intrinsic activity of electrocatalysts in electrochemical water splitting? *ACS Energy Lett.* 4 (2019) 1260–1264, <https://doi.org/10.1021/acsenergylett.9b00686>.
- [12] Y. Song, W. Xie, M. Shao, X. Duan, Integrated electrocatalysts derived from metal organic frameworks for gas-involved reactions, *Nano Mater. Sci.* 5 (2023) 161–176, <https://doi.org/10.1016/j.nanoms.2022.01.003>.

- [13] H. Adamu, M. Qamar, Routes to enhanced performance of electrolytic hydrogen evolution reaction over the carbon-encapsulated transition metal alloys, *J. Electrochem. Sci. Eng.* 12 (2022) 947–974, <https://doi.org/10.5599/jese.1446>.
- [14] H. Wang, P. Yang, X. Sun, W. Xiao, X. Wang, M. Tian, G. Xu, Z. Li, Y. Zhang, F. Liu, L. Wang, Z. Wu, Co-Ru alloy nanoparticles decorated onto two-dimensional nitrogen doped carbon nanosheets towards hydrogen/oxygen evolution reaction and oxygen reduction reaction, *J. Energy Chem.* 87 (2023) 286–294, <https://doi.org/10.1016/j.jechem.2023.08.039>.
- [15] EcoEnergy - 2023 - Zhou - Self-integration exactly constructing oxygen-modified MoNi alloys for efficient hydrogen.pdf, (n.d.).
- [16] C. Zhang, H. Nan, H. Tian, W. Zheng, Recent advances in pentlandites for electrochemical water splitting: A short review, *J. Alloys Compd.* 838 (2020), <https://doi.org/10.1016/j.jallcom.2020.155685>.
- [17] EcoEnergy - 2023 - Sher Shah - Transition metal carbide-based nanostructures for electrochemical hydrogen and oxygen.pdf, (n.d.).
- [18] Q. Li, X. Luan, Z. Xiao, W. Xiao, G. Xu, Z. Li, Z. Wu, L. Wang, Ultrafast microwave synthesis of Ru-doped MoP with abundant P vacancies as the electrocatalyst for hydrogen generation in a wide pH range, *Inorg. Chem.* 62 (2023) 9687–9694, <https://doi.org/10.1021/acs.inorgchem.3c01299>.
- [19] Advanced Energy Materials - 2023 - Yang - Microwave Quasi-Solid State to Construct Strong Metal-Support Interactions with.pdf, (n.d.).
- [20] N. Zdolsek, M. Vujković, Š. Metin, S. Brković, A. Jocić, A. Dimitrijević, T. Trtić-Petrović, B. Šljukić, Boosting electrocatalysis of oxygen reduction and evolution reactions with cost-effective cobalt and nitrogen-doped carbons prepared by simple carbonization of ionic liquids, *Int. J. Hydrogen Energy* 47 (2022) 14847–14858, <https://doi.org/10.1016/j.ijhydene.2022.02.225>.
- [21] N. Zdolsek, R.P. Rocha, J. Krstić, T. Trtić-Petrović, B. Šljukić, J.L. Figueiredo, M. J. Vujković, Electrochemical investigation of ionic liquid-derived porous carbon materials for supercapacitors: pseudocapacitance versus electrical double layer, *Electrochim. Acta* 298 (2019) 541–551, <https://doi.org/10.1016/j.electacta.2018.12.129>.
- [22] A.G. Wallace, M.D. Symes, Water-splitting electrocatalysts synthesized using ionic liquids, *Trends Chem.* 1 (2019) 247–258, <https://doi.org/10.1016/j.trechm.2019.03.003>.
- [23] T. Li, W. Hu, Ionic liquid derived electrocatalysts for electrochemical water splitting, *Green Energy Environ.* 9 (2024) 604–622, <https://doi.org/10.1016/j.gee.2023.06.004>.
- [24] H.J. Niu, L. Zhang, J.J. Feng, Q.L. Zhang, H. Huang, A.J. Wang, Graphene-encapsulated cobalt nanoparticles embedded in porous nitrogen-doped graphitic carbon nanosheets as efficient electrocatalysts for oxygen reduction reaction, *J. Colloid Interface Sci.* 552 (2019) 744–751, <https://doi.org/10.1016/j.jcis.2019.05.099>.
- [25] X.H. Yan, B.Q. Xu, Mesoporous carbon material co-doped with nitrogen and iron (Fe-N-C): High-performance cathode catalyst for oxygen reduction reaction in alkaline electrolyte, *J. Mater. Chem. A* 2 (2014) 8617–8622, <https://doi.org/10.1039/c3ta15300b>.
- [26] S. Akula, M. Mooste, J. Kozlova, M. Käärik, A. Treshchalov, A. Kikas, V. Kisand, J. Aruväli, P. Paiste, A. Tamm, J. Leis, K. Tammeveski, Transition metal (Fe Co, Mn, Cu) containing nitrogen-doped porous carbon as efficient oxygen reduction electrocatalysts for anion exchange membrane fuel cells, *Chem. Eng. J.* 458 (2023), <https://doi.org/10.1016/j.cej.2023.141468>.
- [27] S.Q. Shi, W. Che, K. Liang, C. Xia, D. Zhang, Phase transitions of carbon-encapsulated iron oxide nanoparticles during the carbonization of cellulose at various pyrolysis temperatures, *J. Anal. Appl. Pyrolysis* 115 (2015) 1–6, <https://doi.org/10.1016/j.jaap.2015.05.010>.
- [28] Y. Chen, X.F. Zhang, A.J. Wang, Q.L. Zhang, H. Huang, J.J. Feng, Ultrafine Fe3C nanoparticles embedded in N-doped graphitic carbon sheets for simultaneous determination of ascorbic acid, dopamine, uric acid and xanthine, *Microchim. Acta* 186 (2019), <https://doi.org/10.1007/s00604-019-3769-y>.
- [29] Z. Wen, S. Ci, F. Zhang, X. Feng, S. Cui, S. Mao, S. Luo, Z. He, J. Chen, Nitrogen-enriched core-shell structured Fe/Fe 3C-C nanorods as advanced electrocatalysts for oxygen reduction reaction, *Adv. Mater.* 24 (2012) 1399–1404, <https://doi.org/10.1002/adma.201104392>.
- [30] T. Ahmad, Ascorbic acid assisted synthesis, characterization and catalytic application of copper nanoparticles, *Mater. Sci. Eng. Int. J.* 2 (2018), <https://doi.org/10.15406/mseij.2018.02.00040>.
- [31] G. Zhang, B. Xu, H. Chong, W. Wei, C. Wang, G. Wang, Effect of glyphosate on X-ray diffraction of copper films prepared by electrochemical deposition, *RSC Adv.* 9 (2019) 14016–14023, <https://doi.org/10.1039/c9ra01385g>.
- [32] M. Kumar, V. Bhatt, O.S. Nayal, S. Sharma, V. Kumar, M.S. Thakur, N. Kumar, R. Bal, B. Singh, U. Sharma, CuI nanoparticles as recyclable heterogeneous catalysts for C-N bond formation reactions, *Catal. Sci. Technol.* 7 (2017) 2857–2864, <https://doi.org/10.1039/c7cy00832e>.
- [33] H. Lv, H. Zhao, T. Cao, L. Qian, Y. Wang, G. Zhao, Efficient degradation of high concentration azo-dye wastewater by heterogeneous Fenton process with iron-based metal-organic framework, *J. Mol. Catal. A Chem.* 400 (2015) 81–89, <https://doi.org/10.1016/j.molcata.2015.02.007>.
- [34] K. Ranganathan, A. Morais, I. Nongwe, C. Longo, A.F. Nogueira, N.J. Coville, Study of photoelectrochemical water splitting using composite films based on TiO₂ nanoparticles and nitrogen or boron doped hollow carbon spheres as photoanodes, *J. Mol. Catal. A Chem.* 422 (2016) 165–174, <https://doi.org/10.1016/j.molcata.2015.10.024>.
- [35] S. Bian, X. Li, L. Zhang, L. Wang, J. Wang, Q. Xu, L. Zang, Y. Zhang, L. Sun, Bimetal Cu and Fe modified g-C3N4sheets grown on carbon skeleton for efficient and selective photocatalytic reduction of CO₂to CO, *J. Environ. Chem. Eng.* 11 (2023), <https://doi.org/10.1016/j.jeche.2023.109319>.
- [36] Z.K. Yang, Z.W. Zhao, K. Liang, X. Zhou, C.C. Shen, Y.N. Liu, X. Wang, A.W. Xu, Synthesis of nanoporous structured iron carbide/Fe-N-carbon composites for efficient oxygen reduction reaction in Zn-air batteries, *J. Mater. Chem. A* 4 (2016) 19037–19044, <https://doi.org/10.1039/C6TA08050B>.
- [37] T. Fujii, F.M.F. De Groot, G.A. Sawatzky, F.C. Voogt, T. Hibma, K. Okada, In situ XPS analysis of various iron oxide films grown by NO 2-assisted molecular-beam epitaxy, n.d.
- [38] F. Luo, S. Wagner, W. Ju, M. Prims, S. Li, H. Wang, U.I. Kramm, P. Strasser, Kinetic diagnostics and synthetic design of platinum group metal-free electrocatalysts for the oxygen reduction reaction using reactivity maps and site utilization descriptors, *J. Am. Chem. Soc.* 144 (2022) 13487–13498, <https://doi.org/10.1021/jacs.2c01594>.
- [39] S. Chen, L. Brown, M. Levendorf, W. Cai, S.Y. Ju, J. Edgeworth, X. Li, C. W. Magnuson, A. Velamakanni, R.D. Piner, J. Kang, J. Park, R.S. Ruoff, Oxidation resistance of graphene-coated Cu and Cu/Ni alloy, *ACS Nano* 5 (2011) 1321–1327, <https://doi.org/10.1021/nn103028d>.
- [40] F. Xiao, G.L. Xu, C.J. Sun, M. Xu, W. Wen, Q. Wang, M. Gu, S. Zhu, Y. Li, Z. Wei, X. Pan, J. Wang, K. Amine, M. Shao, Nitrogen-coordinated single iron atom catalysts derived from metal organic frameworks for oxygen reduction reaction, *Nano Energy* 61 (2019) 60–68, <https://doi.org/10.1016/j.nanoen.2019.04.033>.
- [41] Q. Zuo, P. Zhao, W. Luo, G. Cheng, Hierarchically porous Fe-N-C derived from covalent-organic materials as a highly efficient electrocatalyst for oxygen reduction, *Nanoscale* 8 (2016) 14271–14277, <https://doi.org/10.1039/c6nr03273g>.
- [42] L. Bokobza, J.L. Bruneel, M. Couzi, Raman spectroscopic investigation of carbon-based materials and their composites. Comparison between carbon nanotubes and carbon black, *Chem. Phys. Lett.* 590 (2013) 153–159, <https://doi.org/10.1016/j.cplett.2013.10.071>.
- [43] A.C. Ferrari, J.C. Meyer, V. Scardaci, C. Casiraghi, M. Lazzeri, F. Mauri, S. Pisacane, D. Jiang, K.S. Novoselov, S. Roth, A.K. Geim, Raman spectrum of graphene and graphene layers, *Phys. Rev. Lett.* 97 (2006), <https://doi.org/10.1103/PhysRevLett.97.187401>.
- [44] V. Thapliyal, M.E. Alabdulkarim, D.R. Whelan, B. Mainali, J.L. Maxwell, A concise review of the Raman spectra of carbon allotropes, *Diam. Relat. Mater.* 127 (2022), <https://doi.org/10.1016/j.diamond.2022.109180>.
- [45] M.E.G. Lyons, M.P. Brandon, A comparative study of the oxygen evolution reaction on oxidised nickel, cobalt and iron electrodes in base, *J. Electroanal. Chem.* 641 (2010) 119–130, <https://doi.org/10.1016/j.jelechem.2009.11.024>.
- [46] R.L. Doyle, M.E.G. Lyons, Kinetics and mechanistic aspects of the oxygen evolution reaction at hydrous iron oxide films in base, *J. Electrochem. Soc.* 160 (2013) H142–H154, <https://doi.org/10.1149/2.015303jes>.
- [47] V.N. Nikolić, M.M. Vasić, J. Milikić, J.F.M.L. Mariano, The influence of thermal treatment on the formation mechanism of the Cu, Fe-containing nanocomposite material synthesized by the sol-gel method, *Phys. Solid State* 63 (2021) 332–354, <https://doi.org/10.1134/S1063783421020207>.
- [48] Y. Deng, A.D. Handoko, Y. Du, S. Xi, B.S. Yeo, In situ Raman spectroscopy of copper and copper oxide surfaces during electrochemical oxygen evolution reaction: identification of CuII oxides as catalytically active species, *ACS Catal.* 6 (2016) 2473–2481, <https://doi.org/10.1021/acscatal.6b00205>.
- [49] B. Šljukić, M. Vujković, L. Amaral, D.M.F. Santos, R.P. Rocha, C.A.C. Sequeira, J. L. Figueiredo, Carbon-supported Mo2C electrocatalysts for hydrogen evolution reaction, *J. Mater. Chem. A* 3 (2015) 15505–15512, <https://doi.org/10.1039/c5ta02346g>.
- [50] M. Yu, E. Budiyanto, H. Tüysüz, Principles of water electrolysis and recent progress in cobalt-, nickel-, and iron-based oxides for the oxygen evolution reaction, *Angew. Chem., Int. Ed.* 61 (2022), <https://doi.org/10.1002/anie.202103824>.
- [51] M. Li, Y. Xiong, X. Liu, X. Bo, Y. Zhang, C. Han, L. Guo, Facile synthesis of electrospun MFe2O4 (M = Co, Ni, Cu, Mn) spinel nanofibers with excellent electrocatalytic properties for oxygen evolution and hydrogen peroxide reduction, (2015). <https://doi.org/10.1039/c4nr07243j>.
- [52] T. Shinagawa, A.T. Garcia-Esparza, K. Takanabe, Insight on Tafel slopes from a microkinetic analysis of aqueous electrocatalysis for energy conversion, *Sci. Rep.* 5 (2015), <https://doi.org/10.1038/srep13801>.
- [53] A. Damjanovic, A. Dart, M. Bocws, 791 to 814. Pergamon Prm Ltd, 1966.
- [54] D. Mladenović, A. Mladenović, D.M.F. Santos, A.B. Yurtcan, Š. Miljanić, S. Mentus, B. Šljukić, Transition metal oxides for bifunctional ORR/OER electrocatalysis in unitized regenerative fuel cells, *J. Electroanal. Chem.* 946 (2023) 117709, <https://doi.org/10.1016/j.jelechem.2023.117709>.
- [55] S. Anantharaj, S.R. Ede, K. Karthick, S. Sam Sankar, K. Sangeetha, P.E. Karthik, S. Kundu, Precision and correctness in the evaluation of electrocatalytic water splitting: Revisiting activity parameters with a critical assessment, *Energy Environ. Sci.* 11 (2018) 744–771, <https://doi.org/10.1039/c7ee03457a>.
- [56] S.F. Hung, Y.Y. Hsu, C.J. Chang, C.S. Hsu, N.T. Suen, T.S. Chan, H.M. Chen, Unraveling geometrical site confinement in highly efficient iron-doped electrocatalysts toward oxygen evolution reaction, *Adv. Energy Mater.* 8 (2018) 1–11, <https://doi.org/10.1002/aenm.201701686>.
- [57] F. Xu, G. Qian, W. Chen, L. Luo, F. Shen, S. Yin, Copper-iron selenides ultrafine nanowires as cost-effective catalysts for the oxygen evolution reaction at large-current-density, *J. Phys. Chem. C* 124 (2020) 19595–19602, <https://doi.org/10.1021/acs.jpcc.0c04625>.
- [58] C. Ye, Z. Wang, Y. Shen, Preparation of iron-copper oxalates and oxides for the oxygen evolution reaction, *J. Electrochem. Soc.* 169 (2022) 064503, <https://doi.org/10.1149/1945-7111/ac7259>.
- [59] D. Mladenović, E. Daš, D.M.F. Santos, A.B. Yurtcan, Š. Miljanić, B. Šljukić, Boosting oxygen electrode kinetics by addition of cost-effective transition metals (Ni, Fe, Cu)

- to platinum on graphene nanoplatelets, *J. Alloys Compd.* 905 (2022), <https://doi.org/10.1016/j.jallcom.2022.164156>.
- [62] D. Mladenović, E. Daş, D.M.F. Santos, A. Bayrakçeken Yurtcan, B. Šljukić, Highly efficient oxygen electrode obtained by sequential deposition of transition metal-platinum alloys on graphene nanoplatelets, *Materials (Basel)* 16 (2023), <https://doi.org/10.3390/ma16093388>.
- [63] Y. Wu, H. He, Electrodeposited nickel–iron–carbon–molybdenum film as efficient bifunctional electrocatalyst for overall water splitting in alkaline solution, *Int. J. Hydrogen Energy* 44 (2019) 1336–1344, <https://doi.org/10.1016/j.ijhydene.2018.11.168>.
- [64] D. Nam, G. Lee, J. Kim, Effect of phosphorus vacancies on activity of Fe-doped Nickel phosphide by NaBH₄ reduction for efficient oxygen evolution under alkaline conditions, *J. Ind. Eng. Chem.* 123 (2023) 201–208, <https://doi.org/10.1016/j.jiec.2023.03.035>.
- [65] J. Zhang, L. Hao, Z. Chen, Y. Gao, H. Wang, Y. Zhang, Facile synthesis of Co–Fe layered double hydroxide nanosheets wrapped on Ni-doped nanoporous carbon nanorods for oxygen evolution reaction, *J. Colloid Interface Sci.* (2023), <https://doi.org/10.1016/j.jcis.2023.06.199>.
- [66] K. Ram Kumar, T. Maiyalagan, Iron nickel sulphide embedded on multi-walled carbon nanotubes as efficient electrocatalysts for oxygen evolution reaction in alkaline medium, *Ceram. Int.* 49 (2023) 1195–1202, <https://doi.org/10.1016/j.ceramint.2022.09.097>.
- [67] L. Gao, X. Zhong, J. Chen, Y. Zhang, J. Liu, B. Zhang, Optimizing the electronic structure of Fe-doped Co₃O₄ supported Ru catalyst via metal-support interaction boosting oxygen evolution reaction and hydrogen evolution reaction, *Chinese Chem. Lett.* (2022) 108085, <https://doi.org/10.1016/j.cclet.2022.108085>.
- [68] A.I. Inamdar, H.S. Chavan, B. Hou, C.H. Lee, S.U. Lee, S.N. Cha, H. Kim, H. Im, A robust nonprecious CuFe composite as a highly efficient bifunctional catalyst for overall electrochemical water splitting, *Small* 16 (2020), <https://doi.org/10.1002/smll.201905884>.
- [69] L. Yan, B. Zhang, J. Zhu, Y. Li, P. Tsiaikaras, P. Kang Shen, Electronic modulation of cobalt phosphide nanosheet arrays via copper doping for highly efficient neutral-pH overall water splitting, *Appl. Catal. B Environ.* 265 (2020), <https://doi.org/10.1016/j.apcatb.2019.118555>.
- [70] K.S. Bhat, H.S. Nagaraja, In situ synthesis of copper sulfide-nickel sulfide arrays on three-dimensional nickel foam for overall water splitting, *ChemistrySelect* 5 (2020) 2455–2464, <https://doi.org/10.1002/slct.202000026>.
- [71] B. Šljukić, D.M.F. Santos, M. Vujković, L. Amaral, R.P. Rocha, C.A.C. Sequeira, J. L. Figueiredo, Molybdenum carbide nanoparticles on carbon nanotubes and carbon xerogel: low-cost cathodes for hydrogen production by alkaline water electrolysis, *ChemSusChem* 9 (2016) 1200–1208, <https://doi.org/10.1002/cssc.201501651>.
- [72] P. Farinazza Bergamo Dias Martins, P. Papa Lopes, E.A. Ticianelli, V. R. Stamenkovic, N.M. Markovic, D. Strmcnik, Hydrogen evolution reaction on copper: Promoting water dissociation by tuning the surface oxophilicity, *Electrochim. Commun.* 100 (2019) 30–33, <https://doi.org/10.1016/j.elecom.2019.01.006>.
- [73] D. Strmcnik, P.P. Lopes, B. Genorio, V.R. Stamenkovic, N.M. Markovic, Design principles for hydrogen evolution reaction catalyst materials, *Nano Energy* 29 (2016) 29–36, <https://doi.org/10.1016/j.nanoen.2016.04.017>.
- [74] S. Wei, P. Xing, Z. Tang, Y. Wang, L. Dai, Spindle-shaped cobalt-doped iron phosphide anchored on three-dimensional graphene electrocatalysis for hydrogen evolution reactions in both acidic and alkaline media, *J. Power Sources* 555 (2023), <https://doi.org/10.1016/j.jpowsour.2022.232414>.

Further reading

- [45] C. Wu, Y. Qu, Y. Wen, S. Gong, Z. Zhu, Cu and Fe bimetallic heterostructure nanoparticles supported by carbon nanotube for multilayer structure electromagnetic interference shielding composite, *Compos. Struct.* 305 (2023), <https://doi.org/10.1016/j.compstruct.2022.116543>.
- [46] A. Pervikov, A. Khrustalyov, A. Filippov, Y. Mironov, A. Lozhkomoev, M. Lerner, S. Tarasov, Structural, mechanical, and tribological characterization of magnetic pulse compacted Fe–Cu bimetallic particles produced by electric explosion of dissimilar metal wires, *Metals (Basel)* 9 (2019), <https://doi.org/10.3390/met9121287>.